

### 6.3 Convergence properties and discretisation errors

Due to the lack of experimental and numerical studies of fluid-structure interaction problems, it is very difficult to validate the developed coupling strategy. Therefore, here, the created algorithm will be investigated numerically.

#### 6.3.1 Test example: Problem formulation

To examine the convergence properties and the discretisations errors of the implicit coupling method a test example similar to the previous one (section 6.2.2) is chosen. Its geometry description is presented in Figure 6.18. Again, the cylinder has a diameter  $d = 0.006$  m and symmetry conditions are implied on its ends. The same fluid parameters are taken, i.e. the density is  $\rho_{fluid} = 1180$  kg/m<sup>3</sup> and the viscosity is  $\mu = 0.0182$  Pa/s.

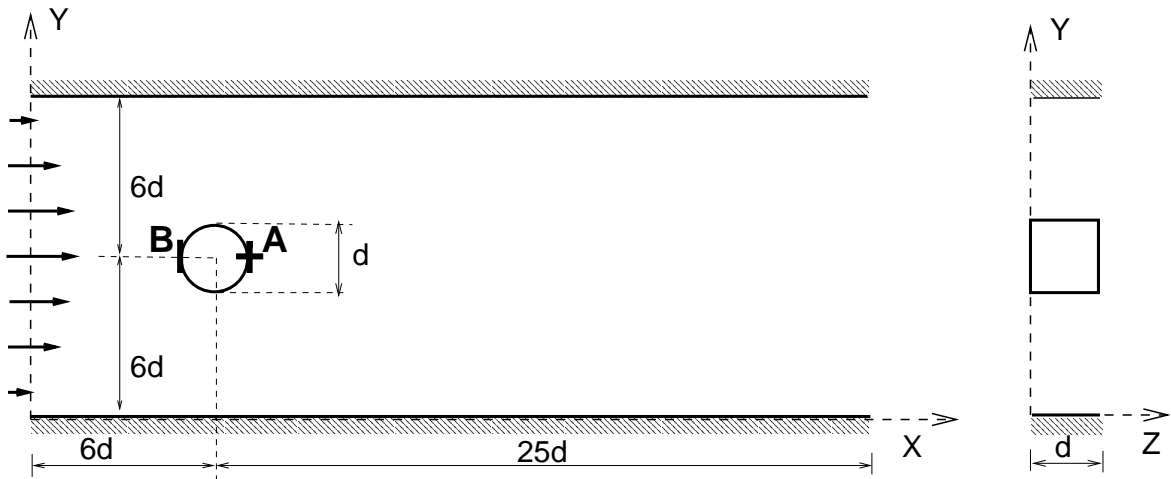


Figure 6.18: Flow around cylinder between two walls - geometry description

However, the boundary conditions used in section 6.2.2 lead to a non-periodic FSI and, finally, to a contact problem for the structure. Therefore, here, the boundary conditions are set so that a periodic FSI is obtained. Contrarily to the example in section 6.2.2 the cylinder is placed in the middle between two walls. The pressure at the inlet coincides to the static pressure, which is also the pressure inside the cylinder. Additionally, at the inlet the analytical solution for a flow between two walls is applied, i.e. the velocity has a parabolic profile. The bulk velocity is chosen  $v_0 = 0.25$  m/s. Hence, the Reynolds number based on the diameter  $d$  of the rigid cylinder is  $Re = 100$ .

To study the properties of the coupling algorithm, three different numerical grids are used to discretise the fluid domain and will be referred as Grid 1, Grid 2 and Grid 3. Grid 1 is the coarsest grid and is depicted in Figure 6.19 (left). It consists of three blocks with  $16 \times 40 \times 6$ ,  $36 \times 104 \times 6$  and  $44 \times 40 \times 6$  CVs respectively and has totally 36864 CVs. The other grids are obtained through consequently refining Grid 1 in x- and y-

grid directions. Along z-direction 6 CVs have been used for all grid levels. Hence, Grid 2 consists of 147456 CVs and Grid 3 - of 589824 CVs.

Let us notice that due to the laminar flow for  $Re = 100$  and the imposed symmetry boundary conditions along the cylinder, the fluid velocity and pressure do not vary in z-direction. Hence, the problem is actually two-dimensional and the number of grid points in the third direction is not important. However, to test the developed coupling algorithm for general three-dimensional problems on a relatively simple example, as well as to use the available solver FASTEST-3D, the fluid dynamics computations will be done in the three-dimensional domain.

On the other hand, since the fluid dynamic forces in z-direction may be neglected, a two dimensional model for the structural computations will be used. Therefore, only a small ring of the cylinder with a height of the z-grid-step, i.e. equal to  $d/6 = 0.001$  m will be considered by the structural subproblem. It is depicted in Figure 6.19 (right). The thickness of the cylinder walls is assumed to be  $d/20$ , i.e.  $3.E-04$  m.

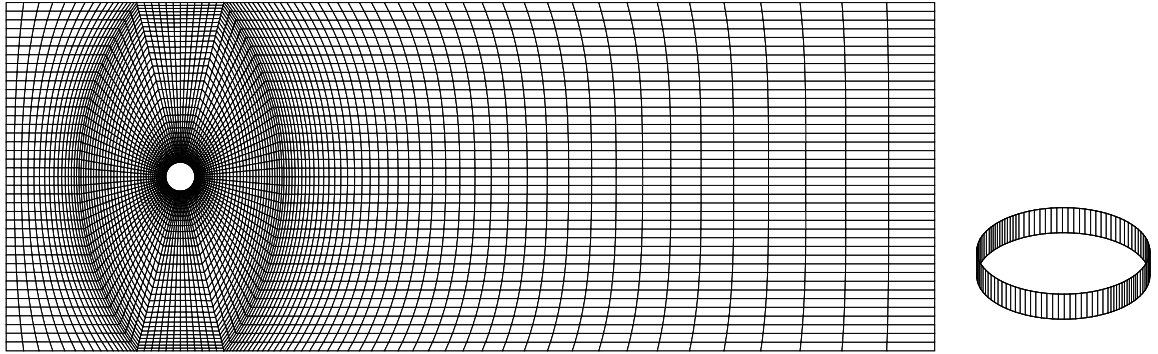


Figure 6.19: Grid 1: Fluid domain (left) and structural domain (right) discretisations

The material is elastic and isotropic with elasticity modulus  $E = 10^4$  kN/m<sup>2</sup>, Poisson ratio  $\nu = 0.42$  and density  $\rho_{struc} = 50000$  kg/m<sup>3</sup>. The cylinder is assumed to be fixed at the back point B and to move only horizontally (i.e. along x) at the front point A as shown in Figure 6.18. In this way, it is assured that no big distortions in the fluid grid can happen due to the cylinder wall deformation.

Frame elements with 3 degrees of freedom (two displacements and one rotation) are used to discretise the considered structure. The grid nodes are extracted from the fluid grid and coincide to the fluid grid points on the cylinder wall on a certain z-level. Hence, correspondingly to the fluid Grid 1, Grid 2 and Grid 3 three discretisations of the cylinder ring are used by the structural subproblem with 104, 208 and 416 frame elements respectively. These elements give a second-order accuracy in space for the structural part. Accordingly, a second-order spatial discretisation for the fluid subtask is achieved implying the central differencing scheme.

To study dynamically the interaction between the flow and the elastic cylinder, four time-steps 0.0005 s, 0.001 s, 0.002 s and 0.004 s will be used.

In order to obtain the periodic vortex street behind a rigid cylinder, a second-order time-stepping scheme is needed. Therefore, the Crank-Nicolson method is taken for time-stepping within the fluid dynamics subproblem. On the other hand the advance in time within the structural solver is realised by the conserving  $\alpha$ -method. The parameters are chosen so that a consistence with the Crank-Nicolson method is achieved.

At the beginning of the simulation, the flow is selected to be the developed periodic flow around the rigid cylinder and will presented in section 6.3.2.

Because finite deformations of the cylinder walls will be considered, the implicit coupling strategy will be applied to the FSI problem. For computational acceleration a two-level multigrid for all considered grids is used, where at each predictor-corrector iteration 5 V-cycles (see section 3.5.2) for the fluid solver are allowed.

### 6.3.2 Fluid dynamics - Discretisation errors.

Before investigating the complete FSI problem, the convergence properties of the fluid part will be studied. For this purpose the test example for a rigid cylinder will be considered.

In order to find the spatial error and the order of convergence for the chosen discretisation schemes for the fluid solver, the calculations will be done on Grid 1, Grid 2 and Grid 3. Additionally, to study the temporal discretisation error, different time-steps will be used.

As it was already pointed out in section 6.2, the dimensionless variables characterising a flow around a cylinder are the drag and the lift coefficients ( $C_D$  and  $C_L$ ) as well as the Strouhal number based on the oscillation period  $T_L$  of the lift coefficient,  $St = d/(v_0 T_L)$ . Hence, these variables have been monitored during the simulations.

All computations have been continued until a periodic state is achieved.

The obtained drag and lift coefficients on the three grids for all used time steps within a time period of 0.1s are visualised in Figures 6.20, 6.21 and 6.22, respectively.

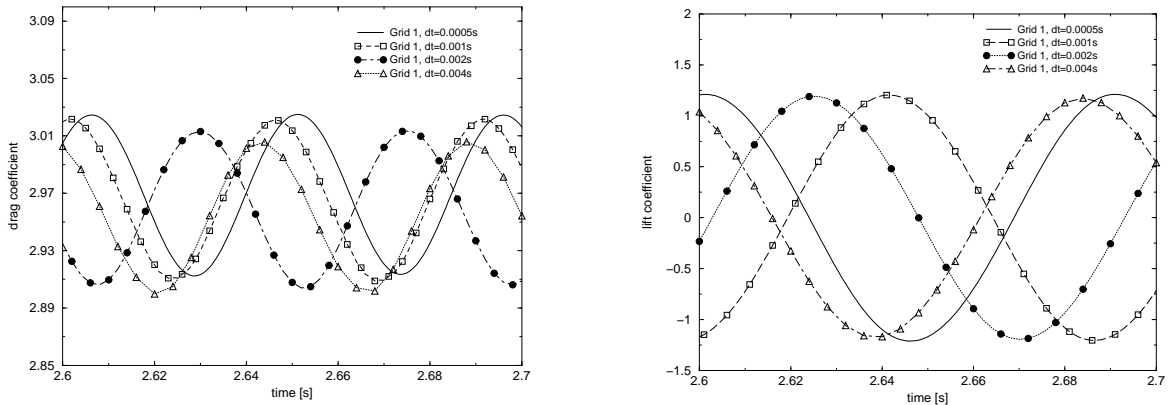


Figure 6.20: Grid 1: Drag (left) and lift (right) coefficients for different time-steps

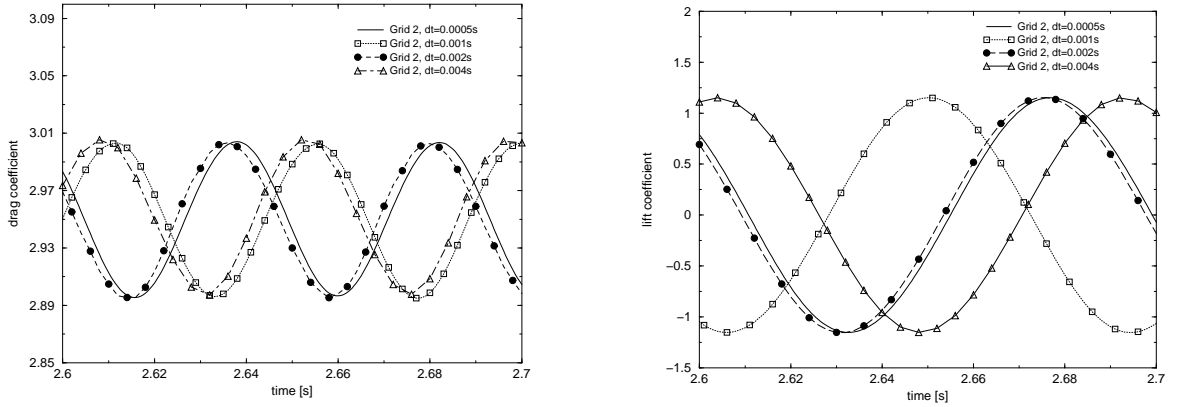


Figure 6.21: Grid 2: Drag (left) and lift (right) coefficients for different time-steps

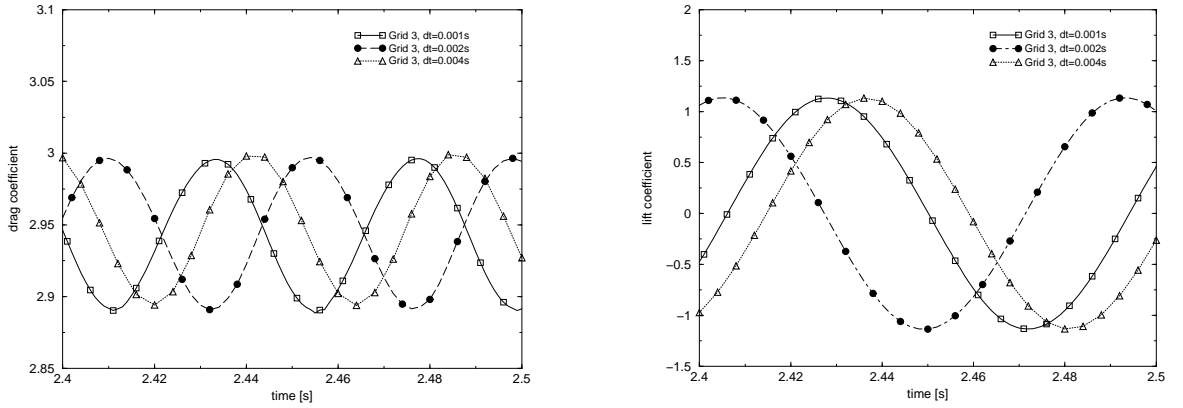


Figure 6.22: Grid 3: Drag (left) and lift (right) coefficients for different time-steps

It can be seen that the values on each grid level lie very close to each other despite the phase offset. For a better comparison the frequencies and the amplitudes of oscillations as well as the average values of the two coefficients will be presented. For this purpose the Fourier transformation has been applied over the data from the last four time-periods  $T_L$ . The obtained results are summarised in Table 6.1. Additionally, the extrapolated time-step independent solution on each grid-level is given. It is evaluated by the linear extrapolation formula of Richardson. This formula may be applied for both spatial and temporal discretisations. If the values  $\phi_{2h}$ ,  $\phi_h$  and  $\phi_{h/2}$  on three consequently refined time- (grid-) levels are available, the order of convergence  $p$  may be found using (6.2):

$$p = \text{Log}_2 \frac{\phi_{2h} - \phi_h}{\phi_h - \phi_{h/2}} \quad (6.2)$$

Then the time-step (grid) independent solution  $\phi$  may be obtained from the Richardson formula (6.3):

$$\phi \approx \phi_h + \frac{\phi_h - \phi_{2h}}{2^p - 1} \quad (6.3)$$

The orders of convergence and the time-step independent solutions on Grid 1 and Grid 2 have been found using the data for time-steps 0.002s, 0.001s and 0.0005s, while on

Grid 3 - the results for time-steps 0.004s, 0.002s and 0.001s. The corresponding relative errors are also presented in Table 6.1 in parentheses below each of the values.

time-step [s] $\Delta t$	lift coefficient			drag coefficient		
	frequency	average	amplitude	frequency	average	amplitude
GRID 1						
0.004	10.989	3.925E-04	1.1732	21.978	2.9535	0.05294
0.002	11.05 (1%)	1.625E-03	1.1919 (2%)	22.099	2.9606 (0.5%)	0.05413 (4.5%)
0.001	11.111 (0.5%)	1.227E-03	1.2038 (1%)	22.222	2.9661 (0.3%)	0.05528 (2.6%)
0.0005	11.142 (0.3%)	-5.809E-04	1.2102 (0.6%)	22.284	2.9695 (0.2%)	0.05592 (1.4%)
indep. solution	11.174	0.0	1.2176		2.9746	0.0567
order	1		0.9		0.7	0.8
GRID 2						
0.004	11.236	1.162E-04	1.1502	22.472	2.9522	0.05445
0.002	11.299	2.865E-04	1.1522 (0.2%)	22.599	2.9501	0.05375
0.001	11.299	8.660E-04	1.1508 (0.07%)	22.599	2.9499	0.05361
0.0005	11.315	3.811E-05	1.1503 (0.02%)	22.631	2.9504	0.05383
indep. solution	-	0.0	1.15		-	-
order	-		1.5		-	-
GRID 3						
0.004	11.236 (1%)	2.048E-03	1.1305	22.472	2.9474 (0.1%)	0.05328 (1.2%)
0.002	11.299 (0.6%)	-2.742E-03	1.1331	22.599	2.9452 (0.04%)	0.05289 (0.4%)
0.001	11.331 (0.3%)	1.175E-03	1.131	22.663	2.9444 (0.01%)	0.05273 (0.02%)
time-step indep. sol.	11.364	0.0	-		2.9439	0.5264
order	1		-		1.5	1.4

Table 6.1: Comparison among the results for the drag and the lift coefficients on Grid 1, Grid 2 and Grid 3 for different time-steps based on the data of four periods  $T_L$

All computations give nearly the same frequencies of oscillations for both coefficients. It can be seen that the frequencies are slightly affected by the spatial discretisation. Grid 2 and Grid 3 are already fine enough for their predictions. Hence, the received frequency

of the lift coefficient is  $1/T_L \approx 11.3$  1/s giving Strouhal number  $St \approx 0.27$  and lift period  $T_L \approx 0.088$ s. The effects of the domain walls on the separating vortices behind the cylinder lead to a higher Strouhal number than that in the example presented in section 6.2.2. The frequency of the drag coefficient is always exactly twice bigger than that of the lift coefficient.

Accordingly, since the cylinder is placed exactly in the middle between the walls, the average lift coefficient is zero with the tolerance of the convergence criterion ( $\varepsilon = 10^{-3}$ ) on all grid levels.

The amplitudes and the average values are also in a very good agreement among each other. They are exactly predicted till the third digit after the decimal point, with an exception of the results for time-step 0.004s. It can be seen in table 6.1 that as the grid is refined, the temporal order of convergence improves. On Grid 3 a time-order of about 1.5 for the average value and the amplitude of the drag coefficient is obtained. Though no order of convergence can be determined for the lift coefficient, it can be noticed that the values received for the used time-steps only slightly differ. However, on Grid 1 and Grid 2 the spatial discretisation errors are still bigger than the temporal ones, which explains the poor convergence on Grid 1.

Temporal order of convergence 1.5 is achieved for the amplitude of the lift coefficient on Grid 2 and the average value and the amplitude of the drag coefficient on Grid 3. Though there is no time order for the other variables, it can be seen that the results on each of the grid levels slightly differ from each other.

To estimate the errors due to the spatial discretisation the results obtained on the three grids are compared for a fixed time-step. For the biggest time-step 0.004s, that is about  $T_L/22$ , no spatial order of convergence may be determined. This is due to the fact that the corresponding time-discretisation errors dominate the errors of the spatial discretisation. The results for the other two time-steps 0.002s ( $T_L/44$ ) and 0.001s ( $T_L/88$ ) are presented in Table 6.2.

Again, it can be seen that the frequency of the lift coefficient is slightly sensitive to the space discretisation. Due to the rather close results on Grid 2 and Grid 3 the spatial order for time-step 0.002s cannot be determined, while it is 2.6 for time-step 0.001s. The relative difference between the frequency on Grid 3 for time-step 0.001s and its predicted grid independent value is only 0.05%.

Let us consider the results for time-step 0.002s. A first order of convergence is achieved for the amplitude of the lift coefficient and the average value of the drag coefficient. Despite the similar amplitudes of the drag coefficient on all grid levels, no order can be determined.

It can be noticed that the spatial order of convergence improves as the time-step is reduced. For time-step 0.001s it is 1.5 for the lift coefficient amplitude and the average drag coefficient. The order for the amplitude of the drag coefficient also exists, but it is only one.

However, the estimated relative errors to the grid independent solution for a fixed time-step show that Grid 3 is fine enough to predict the solution of the fluid problem.

	lift coefficient		drag coefficient	
	frequency	amplitude	average	amplitude
$\Delta t = 0.002s$				
grid indep. solution	-	1.1154	2.94091	-
order	-	1.1	1.1	-
Relative errors (%):				
Grid 1	-	7%	0.7%	-
Grid 2	-	3%	0.3%	-
Grid 3	-	1.6%	0.1%	-
$\Delta t = 0.001s$				
grid indep. solution	11.3376	1.1192	2.9415	0.05177
order	2.6	1.4	1.5	0.91
Relative errors (%):				
Grid 1	2%	7.5%	0.8%	6.7%
Grid 2	0.3%	3%	0.3%	3.5%
Grid 3	0.05%	1%	0.1%	1.8%

Table 6.2: Spatial discretisation errors based on the data of four periods  $T_L$  for time-steps 0.002s and 0.001s

The x-component of the fluid velocity together with the streamtraces on Grid 3 and time-step 0.001s in the whole computational domain are presented in Figure 6.23. There, the Karman vortex street developed behind the cylinder is depicted.

A zoom of the streamtraces and the pressure distribution around the cylinder is given in Figure 6.24. It can be seen that there is an area with a high pressure in front of the body. Two districts with a low pressure appear on the two sides of the cylinder close to the channel walls. As the vortices are consequently formed these two areas alternatively increase and decrease their size.

The study of the discretisation errors showed that Grid 3 and time-step 0.001s are fine enough to predict the fluid dynamics solution. In order to examine the convergence properties of the implicit coupling method for the whole FSI test example, the same spatial and temporal discretisations will be used.

### 6.3.3 Fluid-structure interaction

Before studying the convergence properties of the created implicit coupling algorithm, firstly, the solution of the FSI test example will be found. For this purpose the fluid domain is discretised using Grid 3 and time-step 0.001s is chosen for temporal discretisation.

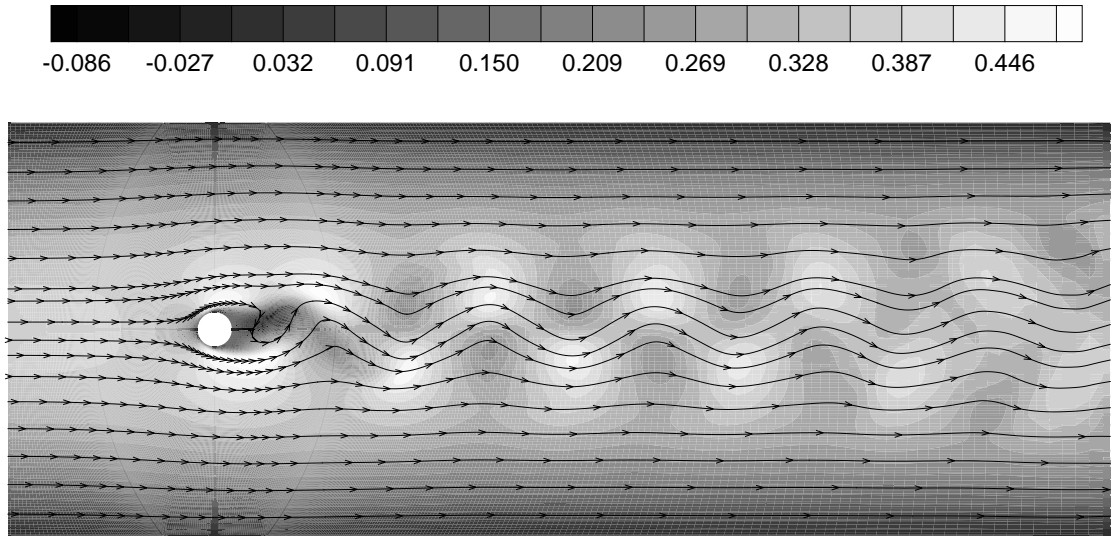


Figure 6.23: Flow around rigid cylinder (Grid 3,  $\Delta t=0.001s$ ): Horizontal velocity and streamtraces

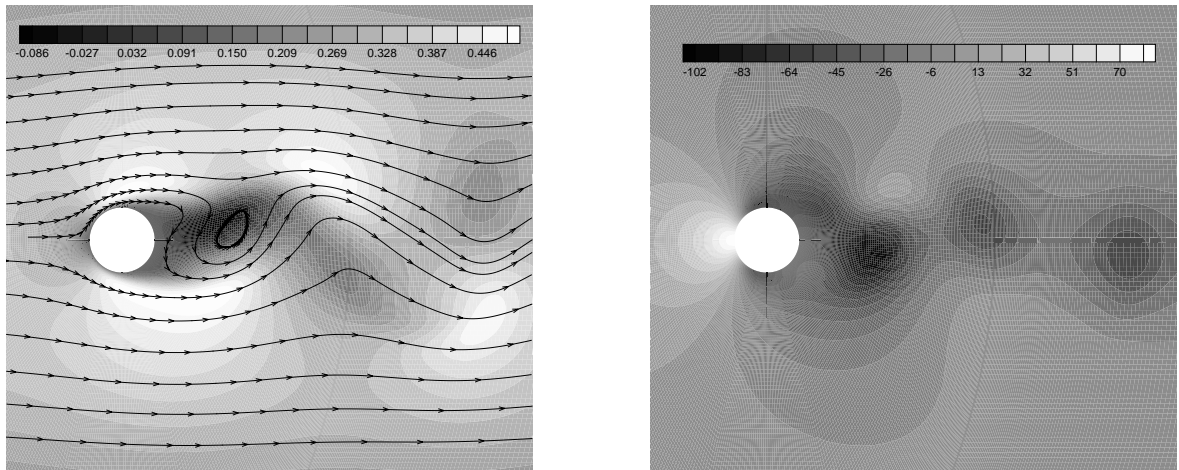


Figure 6.24: Flow around rigid cylinder (Grid 3,  $\Delta t=0.001s$ ): Horizontal velocity and streamtraces (zoom) (left) and pressure distribution (zoom) (right)

Starting from the flow around the undeformed cylinder depicted in Figure 6.23, the interaction between the fluid and the structure is taken into account. In Figure 6.24 (right) the initial pressure distribution around the cylinder is depicted. Obviously, the highest pressure and respectively the biggest fluid force acting on the cylinder are at the point B. Hence, at this point the biggest deformations are expected.

In Figures 6.25 (left) and 6.25 (right) the time history of the drag and the lift coefficients as well as the global horizontal displacement at the point B are shown.

In the beginning the fluid forces strongly deform the cylinder so that the displacement of the point B reaches 2.25 mm. The answer of the structure to the flow decreases

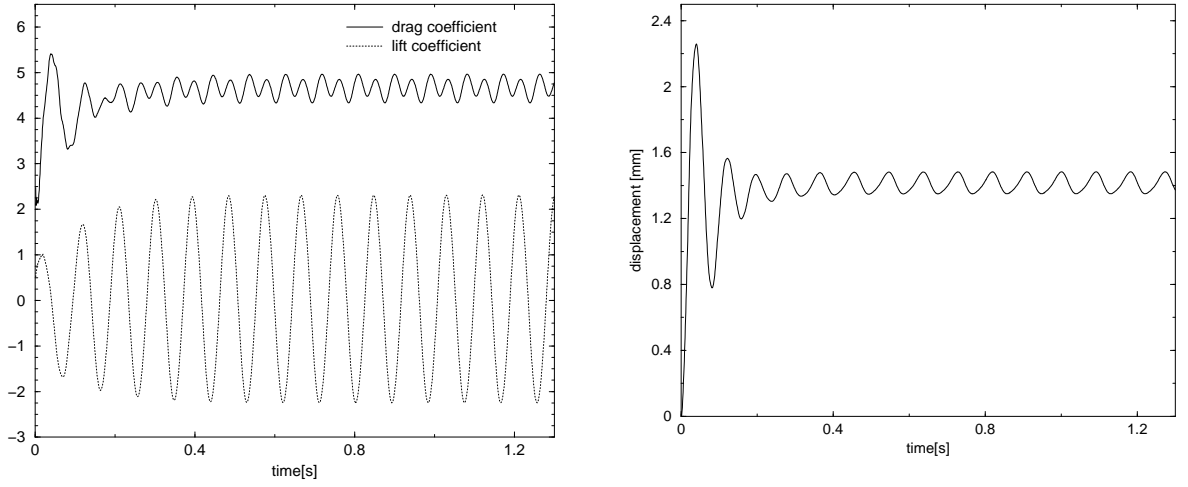


Figure 6.25: FSI time history: Drag and lift coefficients (left) and displacement of point B (right) (Grid 3,  $\Delta t=0.001s$ )

the fluid dynamic forces. Consequently, the displacements of the elastic walls are also reduced. After some development stage, a periodic state is finally reached. The point B of the cylinder moves at a distance of about  $d/4 = 1.5$  mm around which it oscillates due to the fluid forces fluctuations.

From Figure 6.25 (left) two frequencies of oscillation of the drag coefficient are noticed. The drag average value is around 4.66, that is much bigger than the corresponding value 2.94 for a rigid cylinder. This difference is due to the increase of the body surface exposed to the flow, which is caused by the structural deformation.

On the other hand the lift coefficient does not oscillate around zero as it does for a rigid body. The reason is the non-symmetric deformation of the cylinder which will be discussed below.

The frequencies and the amplitudes of fluctuations of the drag and the lift coefficients are found using the fast Fourier transformation over the data from four time-periods and are depicted in Figure 6.26(a).

The frequency of the lift coefficient is  $f_L=1/T_L=11.019$  and the time-period  $T_L=0.09s$ . This gives Strouhal number  $St=(d f_L)/v_0 \approx 0.265$ . Due to the fluid-structure interaction, the obtained frequency is smaller than the one for the rigid cylinder.

Nevertheless, the drag coefficient has again a twice higher frequency than the lift coefficient, i.e.  $2f_L$ . However, due to the interaction with the structure, there is a second frequency exactly equal to  $f_L$  with a significantly smaller amplitude. Accordingly, the horizontal displacement at the point B of the cylinder has the same frequencies as the drag coefficient as it can be seen in Figure 6.26(b). However, since the amplitude of the lift coefficient is much bigger than those of the drag coefficient, the frequency  $f_L$  dominates the structural displacement oscillations.

The achieved periodic cylinder deformation and flow wake on Grid 3 and time-step 0.001s are presented in Figure 6.27. Here, the horizontal velocity and the streamtraces around the elastic cylinder within one period of the lift coefficient are depicted.

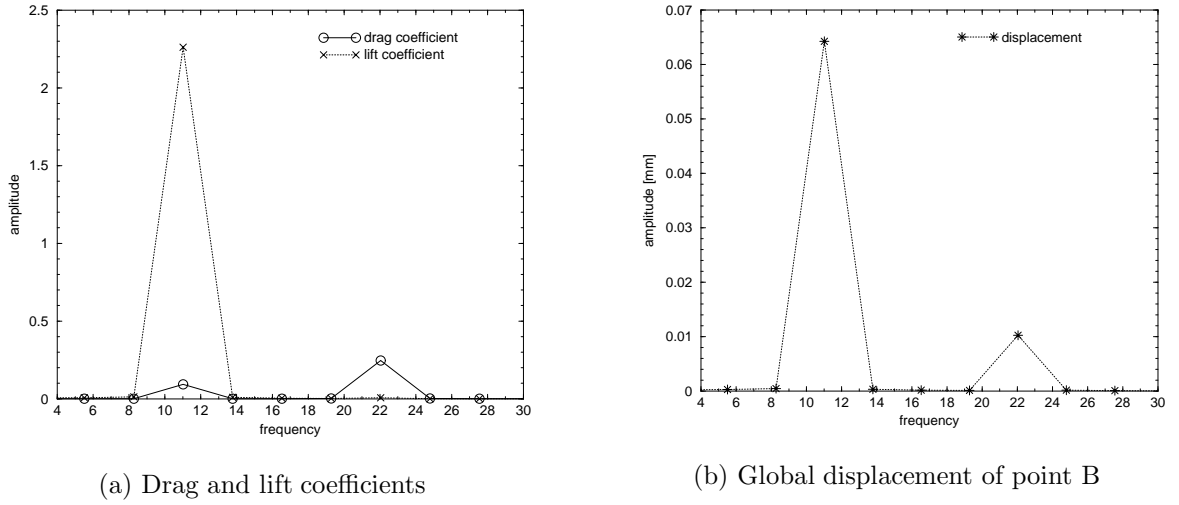


Figure 6.26: Frequencies and amplitudes of oscillations (Grid 3,  $\Delta t=0.001s$ )

The comparison with the flow field around the rigid cylinder in Figure 6.24 (right) shows that the wake behind the elastic cylinder differs from the one behind the rigid cylinder. The dominating drag force deforms the cylinder to a shape similar to an ellipse. Consequently, the surface exposed to the flow increases and a bigger wake behind the deformed cylinder is formed. Hence, the x-component of the fluid velocity reaches a higher value of about 0.64 m/s. Its negative value also significantly reduces to -0.15 m/s behind the cylinder.

The pressure distribution within one period of the lift coefficient is given in Figure 6.28. Similar to the velocity field, it also varies periodically. The areas with a minimum negative pressure correspond to the centers of the travelling vortices.

Due to the time-dependent deformation of the cylinder walls, the volume of the fluid domain changes. Hence, to assure global mass conservation, the outlet mass flux varies despite the constant inlet mass flux. This leads to a bigger range of pressure variation than the one for a rigid cylinder.

In Figure 6.28 it can also be seen that the main deformation of the cylinder is caused by the drag force and is at the point B. However, it turned out that as the vortices are alternatively separating, due to the lift force fluctuations the cylinder also deforms unsymmetrically. At the moment of a vortex formation, the part of the cylinder, where this event takes place, moves in the direction of this vortex. This rather small additional deformation can be noticed at times 0.93s and 0.97s. At these moments the upper and the lower parts of the cylinder correspondingly move in the direction of the flow.

### 6.3.4 FSI - Discretisation errors

To study the implicit coupling algorithm with regard to its spatial and temporal discretisation errors, Grid 1, Grid 2 and Grid 3 are used. The main dimensionless quantities characterising the flow around a cylinder are the drag and the lift coefficients.